Radiative lifetime and Landé-factor measurements of the Se I $4p^3 5s\ ^5S_2$ level using pulsed laser spectroscopy.

Diploma paper by
Raoul Zerne

LRAP-128
Lund, January 1992

investigate by resonance spectroscopy since the the vapor mainly consist of polyatomic molecules. These molecules must be dissociated to make the atomic fraction large enough for spectroscopy. This can be performed in different ways, we have chosen to use differential heating.

Many applications of selenium have been found within semiconductor technology and xerography. Selenium is also known in biology and agriculture as a trace element. Some compounds of selenium are very toxic. Thus it is important to be able to detect small amounts of selenium from a technological as well as from an ecological point of view. It is also of interest to determine the abundance of selenium in astronomical objects. Presently the abundance of selenium in the sun is unknown. In order to assess selenium concentrations from emission measurements it is necessary to know transition probabilities of suitable selenium spectral lines.

2. THEORY

2.1 Lifetime determinations

Excited atoms have different probabilities for decay into different lower states. The spontaneous transition probability for an atom in level i to decay into level k is A_{ik}, and is determined by the matrix element $\langle\Psi_i|e\bar{r}|\Psi_k\rangle$, where $e\bar{r}$ is the electric dipole operator (see Fig. 2.1.1). The total probability for an atom in level i to decay spontaneously, is given by

$$A_i=\sum_k A_{ik} \qquad (2.1.1)$$

where the summation is over all levels, k, with energies less then E_i. If N_0 atoms are excited into level i at time t=0, the number of atoms remaining in this level will decrease exponentially with time

$$N=N_0\exp(-t/\tau_i) \qquad (2.1.2)$$

with

$$\tau_i= 1/A_i. \qquad (2.1.3)$$

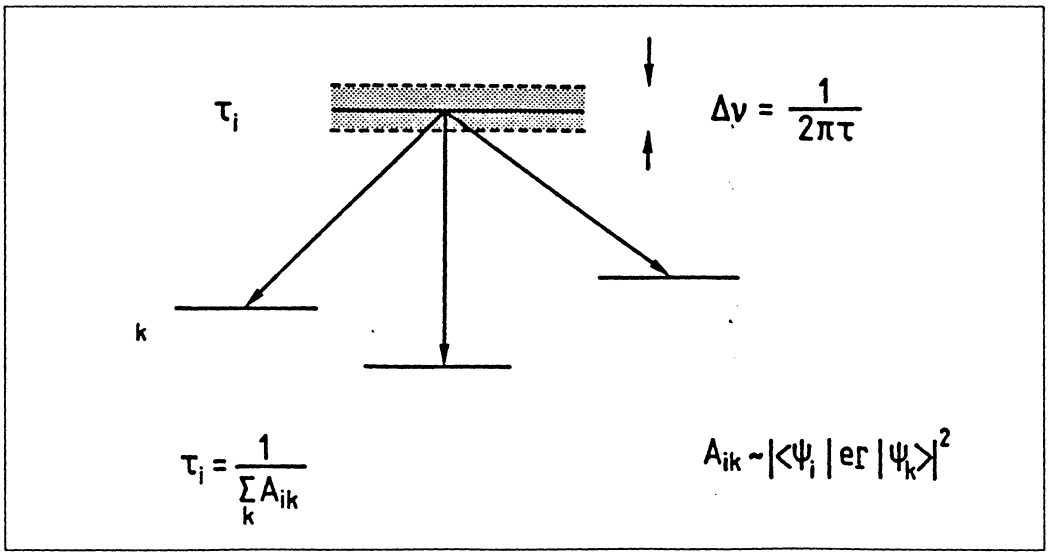

Fig 2.1.1. Relations between radiative properties (From Ref. [1]).

Here we have assumed that the level i is not repopulated from higher levels. This is the bar for the use of emission spectroscopy for lifetimes measurements. The time, on average the atoms remain in level

$$\bar{t} = \frac{\int_0^\infty t\exp(-t/\tau_i)\,dt}{\int_0^\infty \exp(-t/\tau_i)\,dt} = \tau_i \qquad (2.1.4)$$

and therefore τ_i is the mean lifetime for level i. The variance $(\Delta t)^2$ is also easy to calculate

$$(\Delta t)^2 = \frac{\int_0^\infty (t-\tau_i)^2 \exp(-t/\tau_i)\,dt}{\int_0^\infty \exp(-t/\tau_i)\,dt} = \tau_i^2. \qquad (2.1.5)$$

Thus, the "uncertainty" in lifetime is also equal to τ_i. The uncertainty in energy ΔE must fulfill the Heisenberg uncertainty relation

$$\Delta E \cdot \Delta t \geq \hbar/2, \qquad (2.1.6)$$

and the minimum energy uncertainty is $\Delta E_{min} = h/(4\pi\tau)$. The uncertainty in frequency, $\Delta\nu = \Delta E_{min}/h$, defines the natural radiation line width

$$\Delta\nu_N = 2\Delta\nu = 1/2\pi\tau. \qquad (2.1.7)$$

In many cases the individual transition probabilities A_{ik} are of primary interest. There exist several methods for determination of the relative transition probabilities a_{ik}, for example emission spectroscopy (see Table 5.1). Absolute determinations are considerably more difficult. However, lifetime data can be used to determine the normalization constant c

$$\frac{1}{\tau_i} = \sum_k ca_{ik} = \sum_k A_{ik} \qquad (2.1.8)$$

so that the absolute transition probabilities can be determined. Experimental transition probabilities, when compared with theoretical values, provides sensitive testing of theoretical atomic wavefunctions. It is especially sensitive to the outer part of the wavefunctions because of the $\bar{r}$ weighting.

2.2 Quantum-beat through pulsed optical excitation

If the Fourier-limited spectral bandwidth $\Delta\nu \simeq 1/\Delta t$ (Δt pulse lenght) of the laser pulse is larger than the frequency separation of the sublevels $\nu_{12}=(E_1-E_2)/h$ of the excited state, then these sublevels can be populated simultaneously and coherently (see Fig. 2.2.1 a). By coherent we mean that a well-defined relation exists between the phase factors of the different eigenstates. The fluorescence intensity emitted from these coherently prepared sublevels shows a modulated exponential decay. The modulation, or the quantum-beat phenomenon, is due to interference of the transition amplitudes between these different excited states.

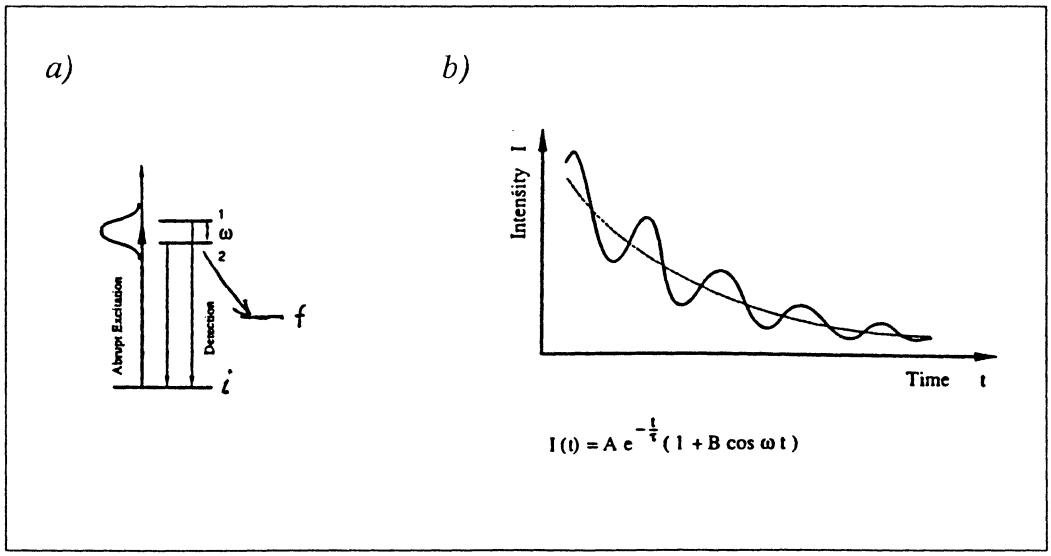

Fig. 2.2.1. Principle of quantum beat (From Ref. [1]). a) Level scheme illustrating coherent excitation of level 1 and 2 with a short broad-band pulse. b) Fluorescence intensity showing a modulation of the exponential decay.

Assume that two closely spaced levels 1 and 2 of an atom or mole-

cule are simultaneously excited by a short laser pulse from a common initial lower level i. If the pulsed excitation occurs at time t=0, the wavefunction of the excited state at this time can be written as a linear superposition of the eigenstates of the excited sublevels:

$$|\Psi(0)\rangle = \sum_k a_k |\phi_k(0)\rangle, \tag{2.2.1}$$

where the coefficients a_k represents the probability amplitudes that the laser pulse has excited the atom into the eigenstate k. Because of the spontaneous decay into the final level f, the wavefunction at a later time t is given by

$$|\Psi(t)\rangle = \sum_k a_k |\phi_k(0)\rangle \exp(-iE_k t/\hbar) e^{-t/2\tau}. \tag{2.2.2}$$

The time-dependent intensity of the fluorescence light emitted from the excited levels is determined by the transition matrix element,

$$I(t) = C|\langle\phi_f|\mathbf{e}_g \cdot \mathbf{r}|\Psi(t)\rangle|^2, \tag{2.2.3}$$

where $\mathbf{e}_g$ is the polarization vector of the emitted fluorescence photon. Inserting (2.2.2) in (2.2.3) yields

$$I(t) = Ce^{-t/\tau}(A + B\cos\omega_{12}t) \tag{2.2.4}$$

with

$$A = a_1^2|\langle\phi_f|\mathbf{e}_g \cdot \mathbf{r}|\phi_1\rangle|^2 + a_2^2|\langle\phi_f|\mathbf{e}_g \cdot \mathbf{r}|\phi_2\rangle|^2, \tag{2.2.5}$$

$$B = 2a_1a_2|\langle\phi_f|\mathbf{e}_g \cdot \mathbf{r}|\phi_1\rangle||\langle\phi_f|\mathbf{e}_g \cdot \mathbf{r}|\phi_2\rangle|, \tag{2.2.6}$$

$$\omega_{12} = (E_2 - E_1)/\hbar. \tag{2.2.7}$$

This shows that a modulation of the exponential decay is observed only if both matrix elements for the transition 1 → f and 2 → f are non zero at the same time. A measurement of the modulation

frequency ω_{12} allow determination of the energy separation of the two levels, even if their energy separation is less than the Doppler width. Quantum-beat spectroscopy therefore allows Doppler-free resolution. This quantum-beat interference effect is analogous to Young's double slit interference experiment. If it had been possible to detect the transitions separately, then the interference effect would have been lost.

Zeeman quantum beats can also be explained semi-classically. The absorbing atoms can be considered as electric dipoles. The linearly polarized radiation from the laser will induce oscillations of the electric dipoles. Oscillating dipoles will radiate in a $\sin^2\theta$ pattern, where θ is the angle relative to the magnetic field. Thus no radiation can be observed in the field direction where the detector is. Since the atom has a magnetic dipole moment it will precess around the magnetic field and the radiation lobe will be turned in towards the detector twice every full revolution.

2.3 Optical double-resonance

The optical double resonance (ODR) method for high resolution spectroscopy was suggested in 1949 by Kastler and Brossel [6]. Two years later, Brossel and Bitter demonstrated the technique on the resonance line of mercury [7]. ODR is primarily used to investigate atomic hyperfine structures and small fine structure, and yield information on the magnetic dipole interaction constant and the electric quadropole interaction constant, also denote as a and b factors. However, ODR also provides a convenient method for determination of the Landé g_J-factor when the life time of the excited state is long.

In optical double-resonance experiments an optical electromagnetic field with frequency ω_{12} and a radio frequency field are simultaneously in resonance with the atoms. An illustrating example is the very first experiment performed by Brossel and Bitter for spin-zero mercury isotopes. The ground state is a $^1S_0$ state, and the

first excited state is a $^3P_1$ state. An external magnetic field will split the first excited state into three magnetic sublevels, but it will leave the ground state unaffected as shown in Fig. 2.3.1 a.

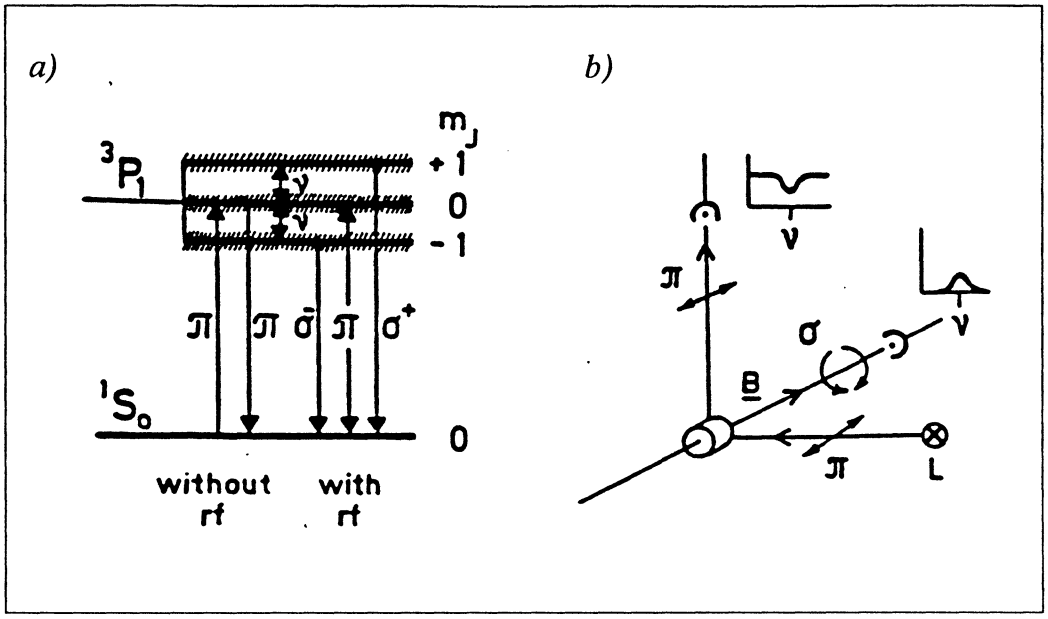

Fig. 2.3.1. Principle of optical double-resonance (From Ref. [1]). a) Zeeman level diagram for spin-zero mercury. b) Schematic experimental setup.

If the optical excitation is made with π-light (the electric field vector of the light is parallel to the external magnetic field), only π-transitions, $\Delta m_J=0$, are induced. The fluorescence light will also contain only π-light, with an angular distribution of the intensity $I_\pi \propto \sin^2\theta$. Thus, no light is emitted in the direction of the external magnetic field. If also the rf field become resonant, then $\Delta m_J=\pm 1$ transitions, are induced and the $m_J=\pm 1$ levels will be populated as well. Since atoms in these states can only decay through σ-transitions ($\Delta m_J=\pm 1$), a strong increase of σ-light and a decrease in π-light will occur. The σ-light has an intensity distribution $I_\sigma \propto (1+\cos^2\theta)$, and has the maximum of the intensity in the direction of the external magnetic field. The rf-field resonance can then be observed with a detector in the external field direction, which will register an increase, or with one in the perpendicular direction, which will register a decrease (see

Fig.2.3.1 b).

The fundamental advantage of the ODR technique, is that the frequency of the rf-field is so low that the Doppler width of the ODR signal becomes much smaller than the natural line width of the optical transition. Even when a Doppler-broadened medium and rather broad-band lasers are used, the resolution obtained is in practice only limited by the Heisenberg uncertainty relation. This is due to the fact that typical rf frequencies are 10^6-10^8 times lower than those of visible light and the Doppler width will be reduced by the same factor, and thereby becomes negligible [1]. When ODR spectroscopy is used in the pulsed version, the resolution may even be increased "beyond" the Heisenberg limit, using delayed detection. The detection system is activated after a certain delay such that only the excited atoms that have survived the longest will contribute to the signal.

The shape and width of the double resonance signal as a function of the frequency of the applied rf-field depend on the natural radiative lifetime τ of the excited state, as well as the amplitude of the rf field [8,10]. In the limit of zero rf field amplitude the curve has Lorentzian shape, and the lifetime τ is given by

$$\tau = \frac{1}{\pi\Delta\nu}, \qquad (2.3.1)$$

where $\Delta\nu$ is the signal full halfwidth. For larger amplitudes the signal will become wider, approximately proportional to the square of the rf amplitude. At even larger amplitudes it becomes distorted, Fig. 2.3.2.

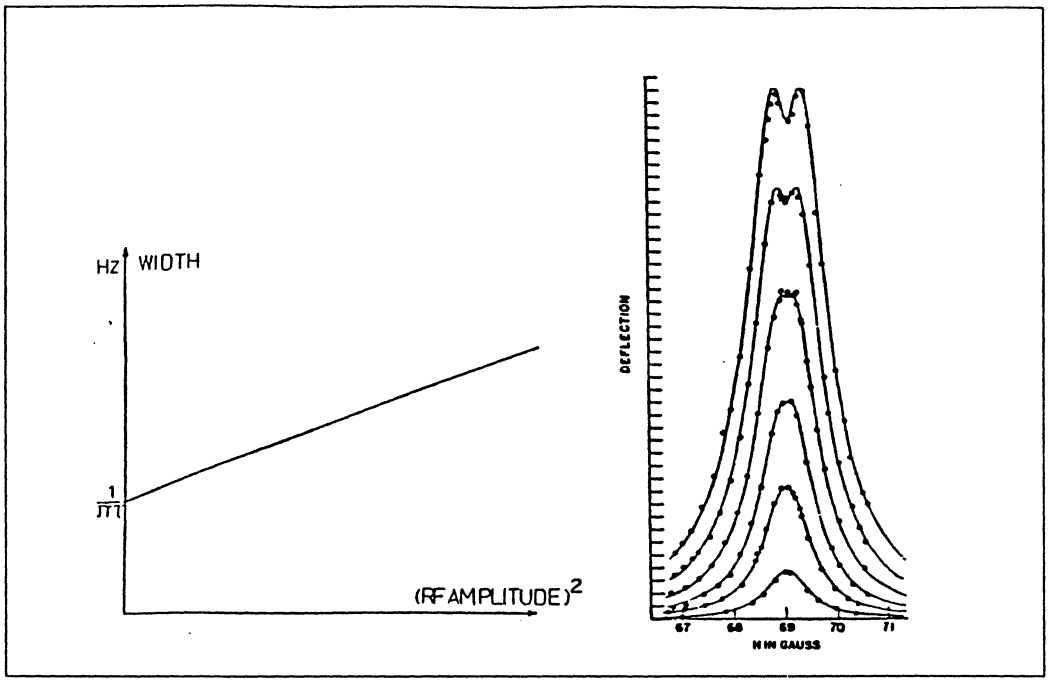

Fig. 2.3.2. Lineshape of double resonance signal for increasing rf amplitude (From *Ref. [7]*).

3. EXPERIMENTS

3.1 The cell arrangement

Selenium resonance cells of quartz glass were manufactured for this experiment following the procedure used in Ref. [5]. Quartz glass is required because the resonance lines fall in the far ultra-violet spectral region and also because of the rather high temperature needed in the experiments. The cell consist of a cylinder, 30 mm in diameter and 40 mm long, to which a 16 cm long stem is attached. A small amount of selenium was first distilled into the cells, so that all impurities of higher boiling temperatures were left behind in the vacuum system. Then the cells were baked out at 750 ^{o}C in high vacuum for about 15 hours. Finally they were sealed off. Natural selenium, consisting of 92 % even-even isotopes (A=74, 76, 78, 80, and 82) and 8 % of ^{77}Se (nuclear spin I=1/2) was used for the cells. Even-even isotopes do not give rise to hyperfine structure since there is no nuclear spin.

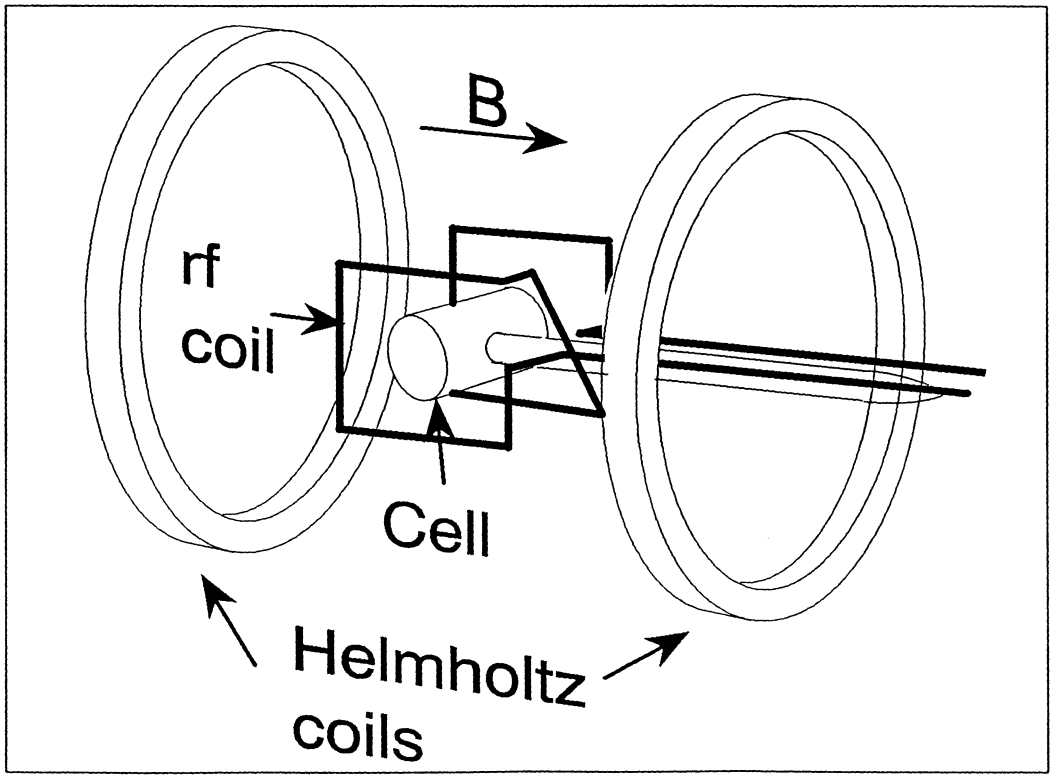

Fig 3.1.1. The cell arrangement.

During the experiments the cells were placed in a differentially heated oven, allowing the cell cylinder to be kept at 100 - 200 ^{o}C higher temperature than the stem. The coldest point determines the total vapor pressure in the cell. To avoid disturbing collisions it is desirable to keep the pressure in the cell as low as possible while retaining a acceptable signal level. The cell arrangement is shown in Fig.3.1.1. In order to obtain free atoms, the molecules had to be thermally dissociated, which demanded a high temperature. The relation between vapor pressure and temperature is given in Fig 3.1.2, but the pressure was more accurately calculated using values from Ref. [13].

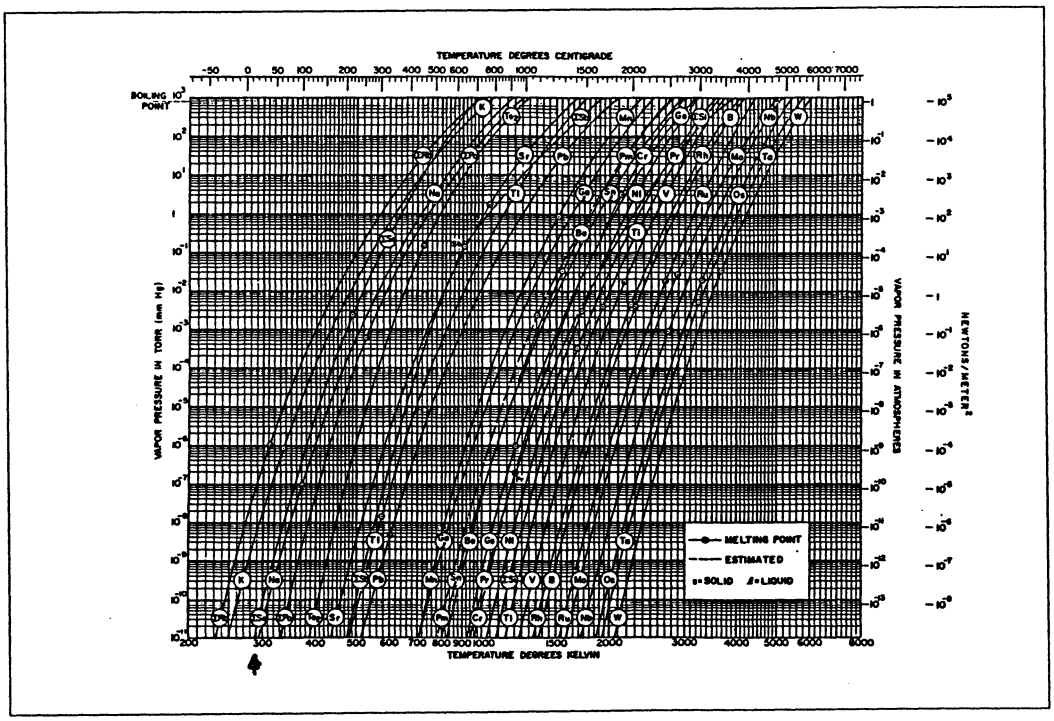

Fig. 3.1.2. Vapor pressure data for some elements (From Ref.[1]). The selenium curve is indicated.

3.2 Experimental setup

The experimental setup is shown in Fig. 3.2.1. The oven was made from non-magnetic materials (including the heating wire, which was made out of platinum) and was placed in a Helmholtz coil system producing a very well-defined magnetic field. A calibration was

performed using optical pumping in ^{133}Cs (see Chap. 4). The temperatures were measured with thermocouples. A Nd:YAG-pumped dye laser delivered high-power pulses of tunable radiation of about 10 ns duration at a repetition rate of 10 Hz. In order to reach the short excitation wavelength around 207 nm, the dye laser radiation at about 621 nm was first frequency doubled in a KDP (potassium dihydrogen phosphate) crystal and then mixed with the fundamental frequency in a BBO (β-barium borate) crystal to effectively produce the third harmonic of the dye-laser frequency. To make the mixing possible a mechanically compressed crystalline quartz plate was used to rotate the fundamental and the doubled dye- laser radiation to obtain parallel polarization components before the BBO crystal. In these experiment pulse energies of about 2 mJ were generated. Fluorescence light on the 216 nm selenium line was isolated with a grating monochromator and was detected by a Hamamatsu R331 photomultiplier tube. During the lifetime measurements and in the quantum-beats experiments, the signals were captured and avereraged with a Tektronix Model DSA 602 transient digitizer and were transferred to an IBM-compatible computer for evaluation.

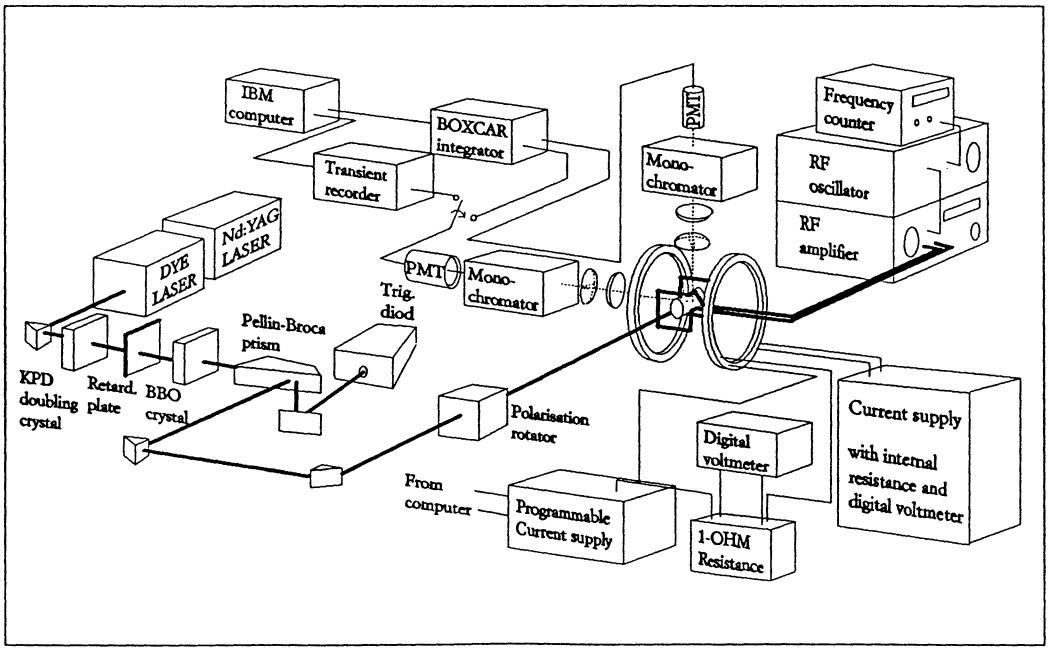

Fig 3.2.1. The experimental set-up used in the lifetime measurements, quantum beats and optical double resonance experiments.

In the ODR experiment, the oven was placed in two pairs of Helmholtz coils producing a well defined magnetic field. One pair of coils was used to produce a static off-set field from which a periodic sweep field could be generated with the second pair. Rf-radiation was provided by a two-turn coil connected to the output of a General Radio 1215-C unit oscillator, amplified in a Boonton Radio 230A tuned amplifier. The fluorescence was detected in two directions. A Stanford Research SR 265 boxcar integrator connected to an IBM-compatible AT computer was used for data collection and processing.

3.3 Lifetime measurements

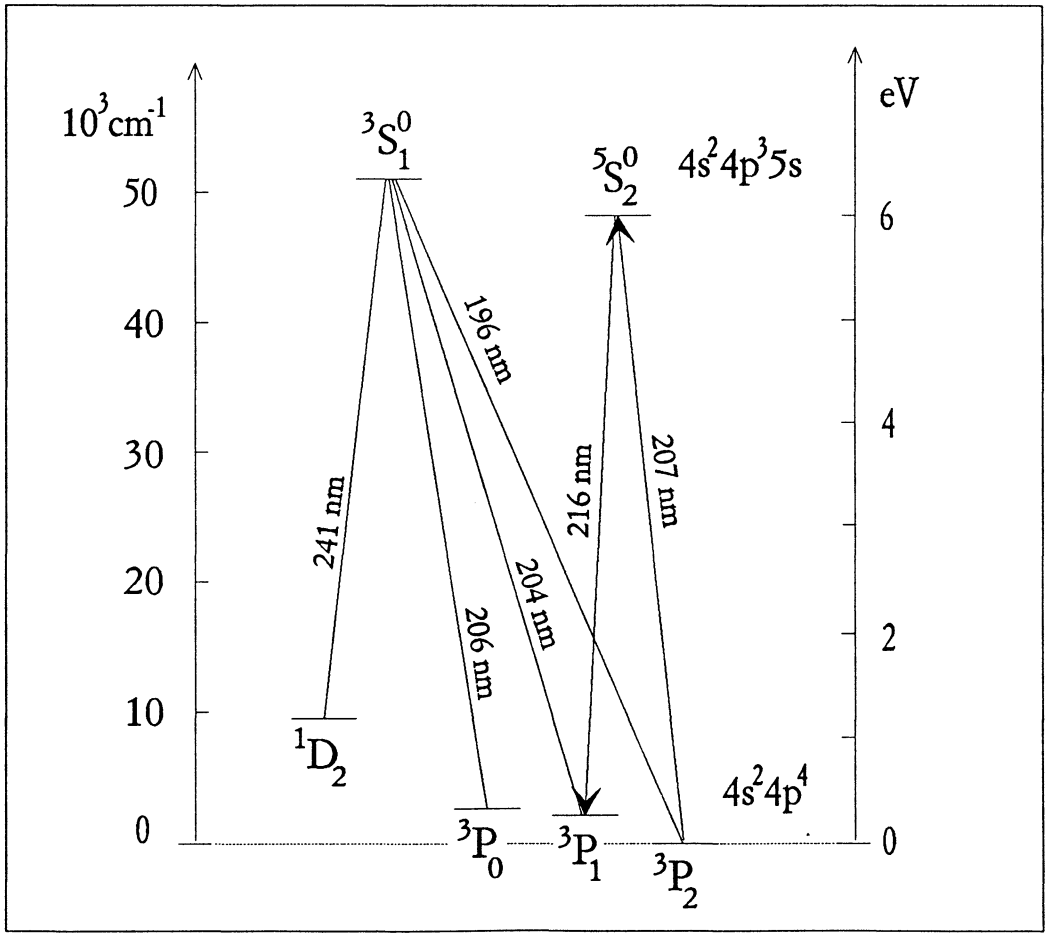

Fig. 3.3.1. Partial energy-level diagram and spectral lines for the selenium atom.

The $4p^35s\ ^5S_2$ level was excited from the $4p^4\ ^3P_2$ ground state and

the fluorescence decay to the $4p^4\ ^3P_1$ level was detected (see Fig. 3.3.1).

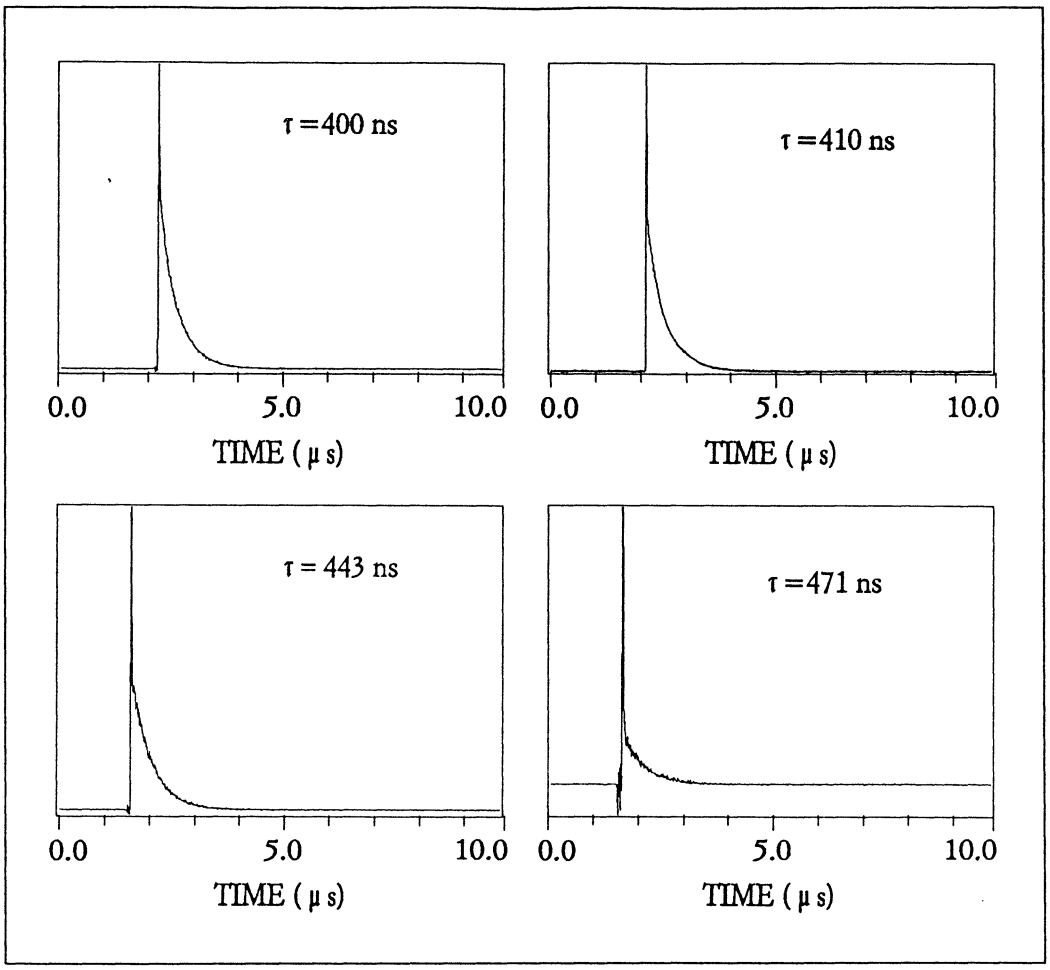

Fig. 3.3.2. Examples of some exponential decays for different temperatures.

Lifetime measurements were performed in a magnetic field strong enough to wash out any quantum-beats due to the earth magnetic field. Slow beats could otherwise cause deviations from a pure exponential decay of the excited state, Fig 3.3.2. Series of recordings were taken for decreasing and increasing cell temperatures and the evaluated inverse lifetime (the decay constant) was plotted as a function of the total selenium pressure as shown in Fig. 3.3.3. The extrapolated value at zero density yields the true radiative lifetime, that was found to be

$$\tau(4p^3 5s\ ^5S_2) = 493(15)\ \text{ns} \qquad (3.3.1)$$

The uncertainty of the value reflects the statistical scatter in the data and also somewhat by the uncertainties in the temperature measurements.

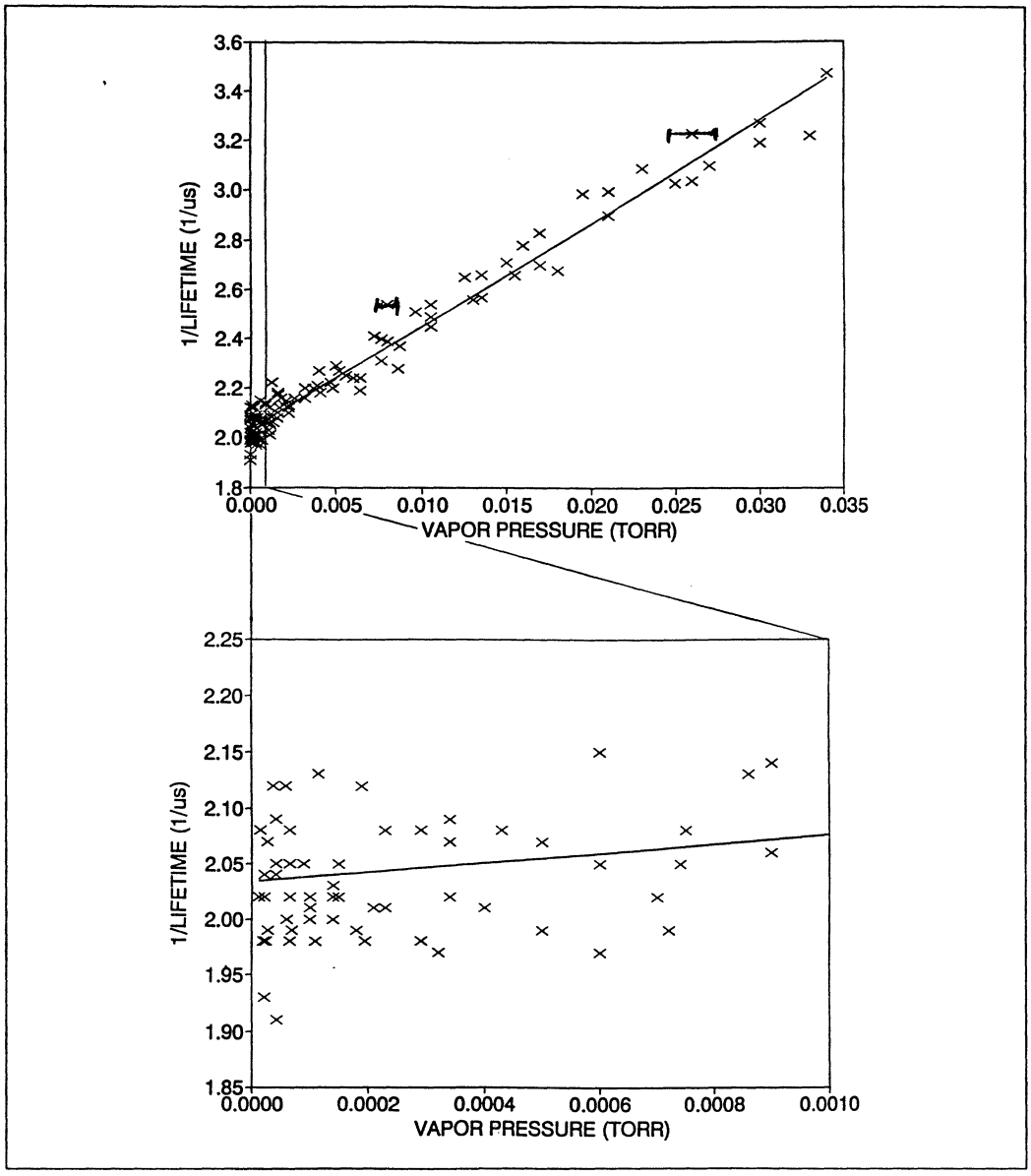

Fig. 3.3.3. Measured decay constant for the $4p^3 5s\ {}^5S_2$ level of selenium as a function of selenium vapor pressure. The change in vapor pressure corresponding to a 1 °C temperature change is indicated.

We note, that the measured lifetime is quite long. Considering that the measurements were performed in a sealed-off cell without

possibilities of further evacuation, the question arises whether the value might be shortened by collisions with residual rest gas in the cell present also in the cold cell. This question is of special interest. First we note, that the same lifetime value was obtained using two different cells, prepared at the same time. Even after artificial aging of one of the cells by heating the cell to 600 ^{o}C for about 5 hours, the lifetime was unaffected. If there had been residual rest gas in the cells, then the plots should have an tendency of flattening out for low temperatures. No such tendency could be observed in plots such as the one in Fig. 3.3.4. Instead the plots were found to be linear over three orders of magnitude of vapor pressure. As an another test we measured the decay times for different combinations of linearly polarized light for excitation and detection, including the "magic angle" (54.7^{o}). It can be shown that the alignment is proportional to $3\cos^2\theta-1$, where θ is the angle between the polarizers in the exciting and detection beams. If the decay was influenced by collisions the measured decay constant should have been dependent on polarizations, since different "alignment moments" would have shown different decay constants [13,14]. However, extrapolations to zero selenium vapor pressure yielded the same lifetime, independent of the setting of the polarizer. A further test was made, where different decay constants for alignment and population were assumed. The function

$$I(t) = A\exp(-t/\tau_1) + B\exp(-t/\tau_2)\cos\omega t \qquad (3.3.2)$$

was fitted to the experimental curves, and the inverse of τ_1 and τ_2 were plotted against the vapor pressure, Fig. 3.3.4. The crossing of the two curves would have determined the true lifetime. However, the two curves coincide and no difference between τ_1 and τ_2 exists. This result, and the result of the "magic angle" tests may be explained by the fact that the measured state is an spherically symmetric S-state which cannot be aligned. The collisions will then affect the alignment and the population decays in the same way. It would be interesting to use the last method for an non S-state.

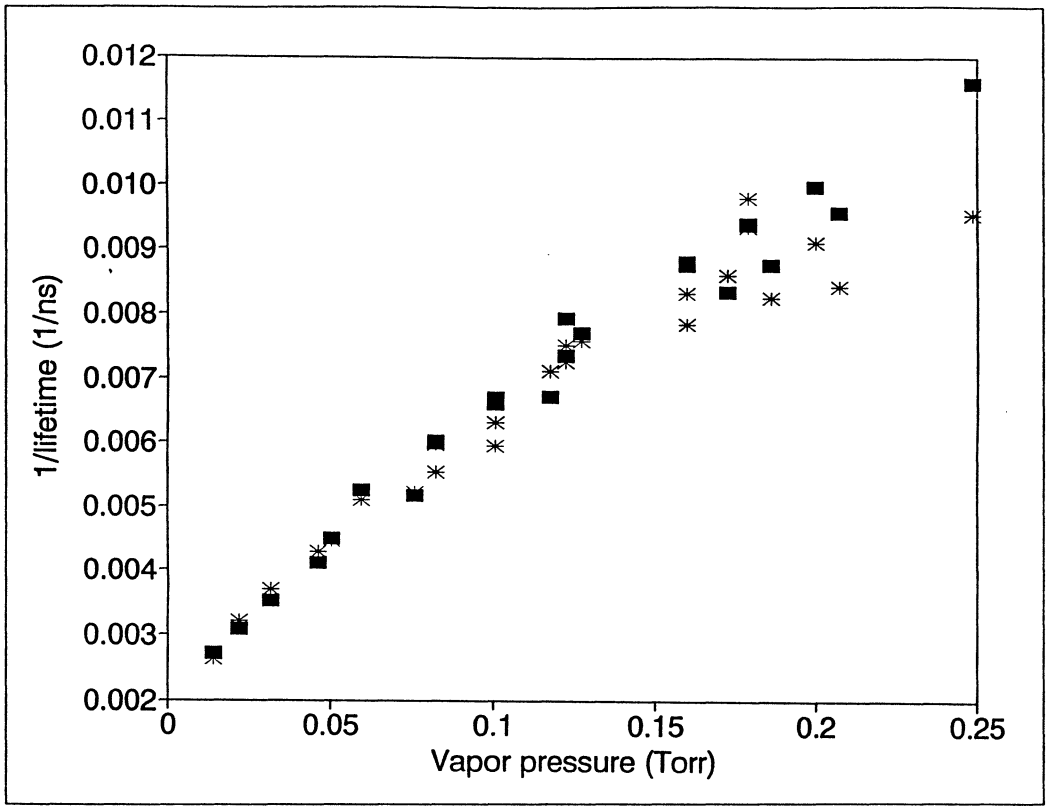

Fig. 3.3.4. Measured decay constants for alignment and population as a function of vapor pressure. The filled squares represent the population and the asterisks represent the alignment decay constants.

3.4 Quantum-beat measurements

In the quantum-beat measurements linearly polarized light with the polarization direction perpendicular to the static magnetic field light was used for excitation. This light therefore consists of both σ^+ and σ^-. The Landé g_J-factor was measured by observing $\Delta m_J = 2$ Zeeman quantum beats, and by optical double resonance experiments. All measurements were performed in a well-defined external magnetic field. The fine structure Zeeman levels are given by

$$E_m = \mu_B g_J m_J B, \qquad (3.4.1)$$

and together with ekv. 2.2.7 the g_J factor can be determined

$$g_J = \frac{\hbar \omega_{12}}{\mu_B \Delta m_J B} \tag{3.4.2}$$

where ω_{12} is the modulation frequency of the quantum-beat. The QB-method can also be used in hyperfine structure studies and will yield information about the a and b factors and the corresponding g_F factor. In ^{77}Se, with I=1/2, there will be two peaks in the Fourier transformed spectra as these in Fig. 3.4.1. The peaks are located one on each side of the g_J peak, since in the Zeeman hyperfine structure levels

$$E_m = \mu_B g_F m_F B, \tag{3.4.3}$$

where the g_F plays the same role as g_J in fine structure. Some attempts to determine the g_F factor of the odd isotope ^{77}Se was made. However, the amount (8 %) was too low and the two peaks were drowned in the noise.

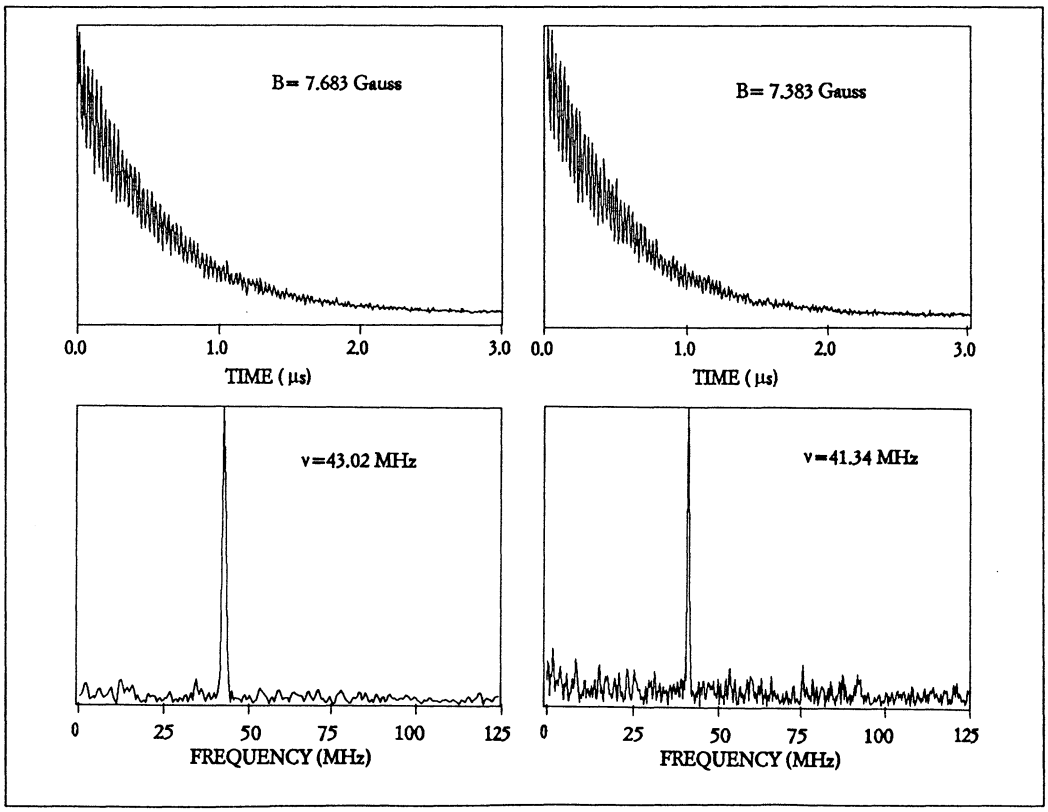

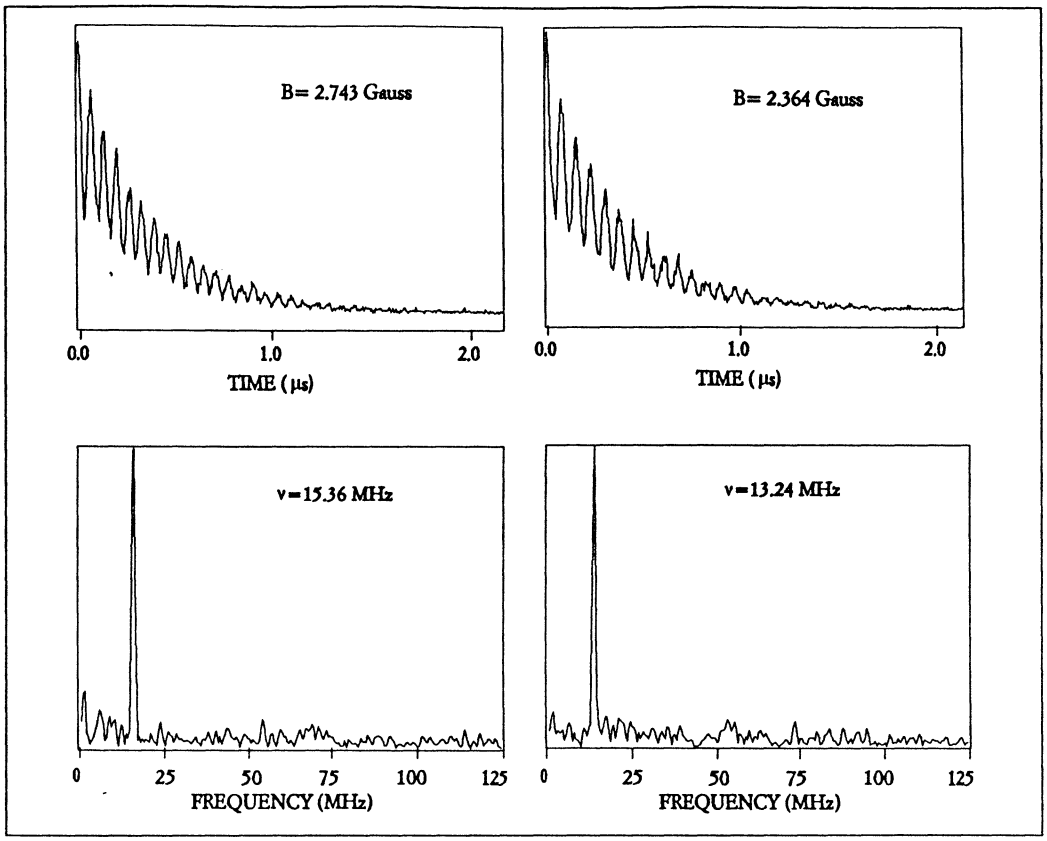

Fig. 3.4.1. Some examples of quantum-beat for two different imposed magnetic field.

Some examples of quantum-beat recordings are shown in Fig. 3.4.1 together with their Fourier transforms yielding the beat frequency. We were not able to obtain the desired accuracy in the quantum-beat measurements, since the Fourier-limited spectral bandwidth ($\Delta\nu \simeq 1/\Delta t$) of the pulse ($\Delta t = 10$ ns) was not large enough and the time response of the experimental setup was not fast enough to allow measurements in the higher magnetic field that would have been required.

3.5 Optical Double-Resonance measurements

The most precise determination of the Landé g_J-factor was made in the optical double-resonance measurements. In an external magnetic field the $4s^2 4p^4\ {}^3P_2$ ground state is split up into five magnetic sublevels. The excited state $4s^2 4p^3 5s\ {}^5S_2$ is also split up into

five sublevels and the final state $4s^2 4p^4\ {}^3P_1$ is split up into three sublevels as shown in Fig 3.5.1. Using π excitation ($\Delta m_J = 0$), the ${}^5S_2$ sublevels were populated and the fluorescence light emitted during the transition to the ${}^3P_1$ sublevels was detected in two directions. π radiation was detected by the main detector and a combination of π and σ radiation was detected by the second detector. The detector arrangement is shown in Fig. 2.3.1. The signals from the two detectors were divided. The reasons for doing this were problems with rather large pulse-to-pulse fluctuations in the laser, and the sensitivity to temperature fluctuations. The heating could not be used during data collection, since the current through the heating wire was produced a disturbing field. When the heating was turned off, the decreasing temperature caused the signal to change in time.

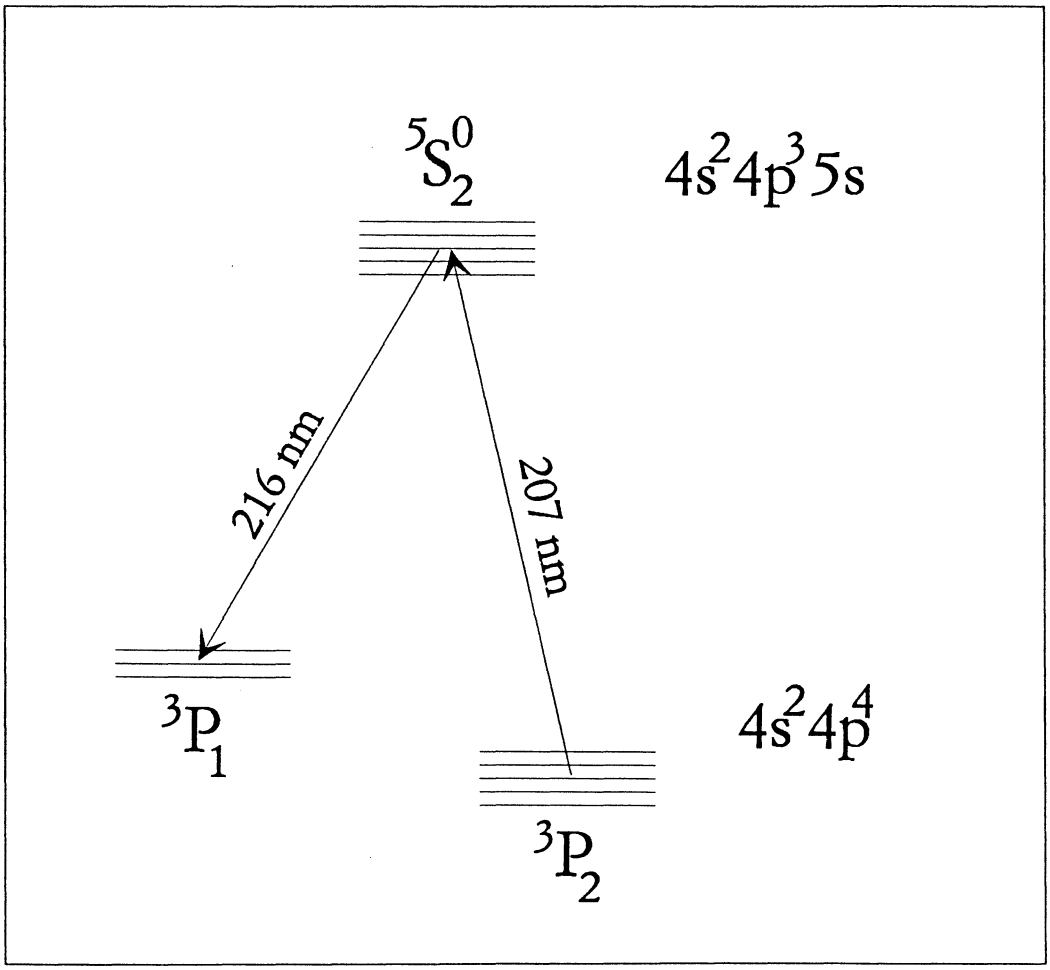

Fig. 3.5.1. Partial energy-level diagram for Zeeman splitting in the selenium atom.

Without quantum-mechanical calculations it is not possible to determine from the energy level diagram in Fig 3.5.1 whether the ODR signal will increase or decrease, when resonant magnetic dipole transitions ($\Delta m_J = \pm 1$) are induced by the rf field. In the experiment it was shown that in the main detector the signal decreased, and in the other direction the signal was unaffected.

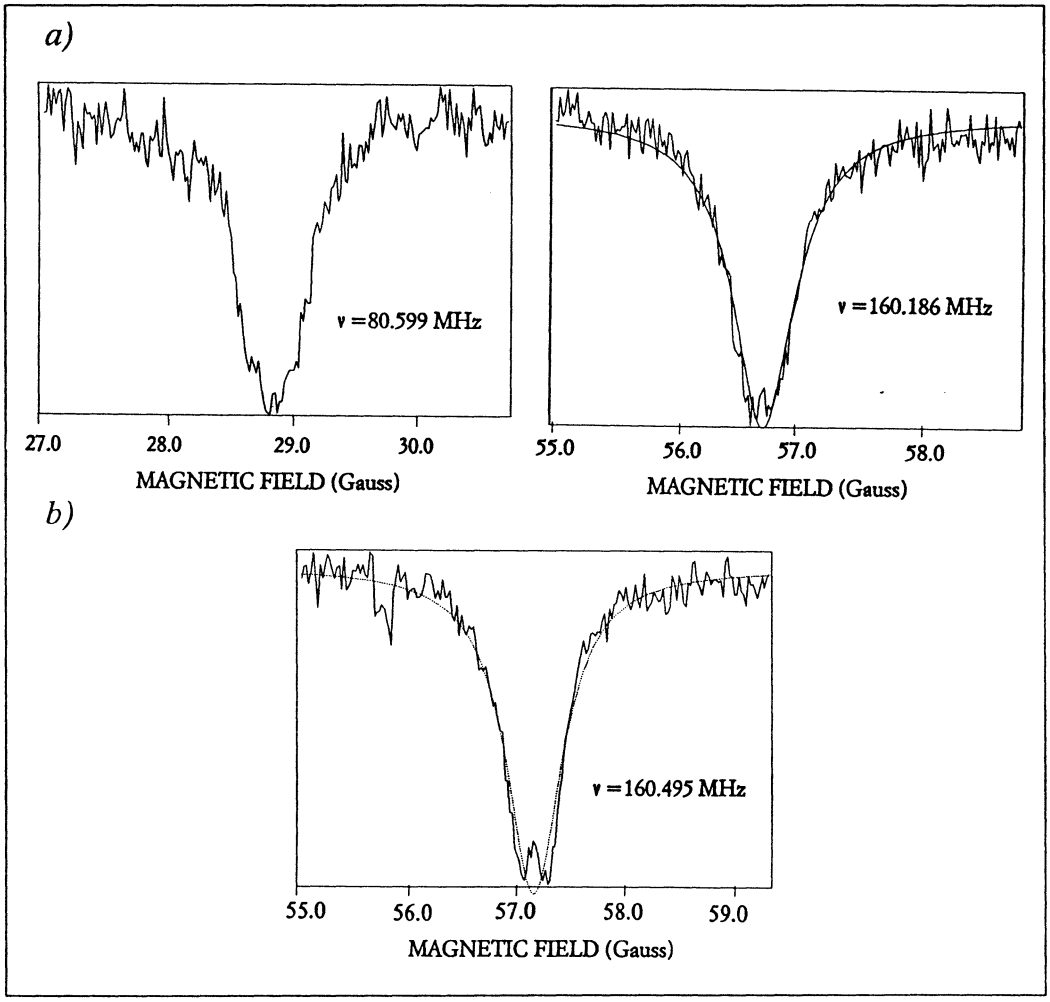

Fig. 3.5.2. a) Three examples of ODR signals. The dotted curves are the fitted functions b) A rf disturbed ODR signal where the characteristic double peak can be seen.

For practical reasons, the magnetic field was swept rather than the rf frequency. Only one peak could be observed, since the even-even isotopes have $I=0$ ($2I+1$ peaks) and the amount of the ^{77}Se isotope is low. The Landé g_J factor can be calculated from the position of the resonance signal, produced when the splitting bet-

ween the equidistant Zeeman levels in the external field B is matched by an rf field of frequency ν

$$g_J = \frac{\nu}{B\mu_B/\hbar} \tag{3.5.1}$$

where $\mu_B/h = 1.39960$ MHz/Gauss. In Fig. 3.5.2 the optical-double resonance signals are shown for a resonance frequency of about 80 and 160 MHz. From the optical double resonance measurements we obtain

$$g_J(4p^3 5s\ ^5S_2) = 2.0004(10). \tag{3.5.2}$$

This value is consistent with the less accurate value obtained in Zeeman quantum-beat experiment. The error is determined by statistical scattering and by an magnetic field calibration (see Chap. 4). Delayed detection measurements were also performed, but without any improvement in accuracy. An example of delayed detection is shown in figure 3.5.3.

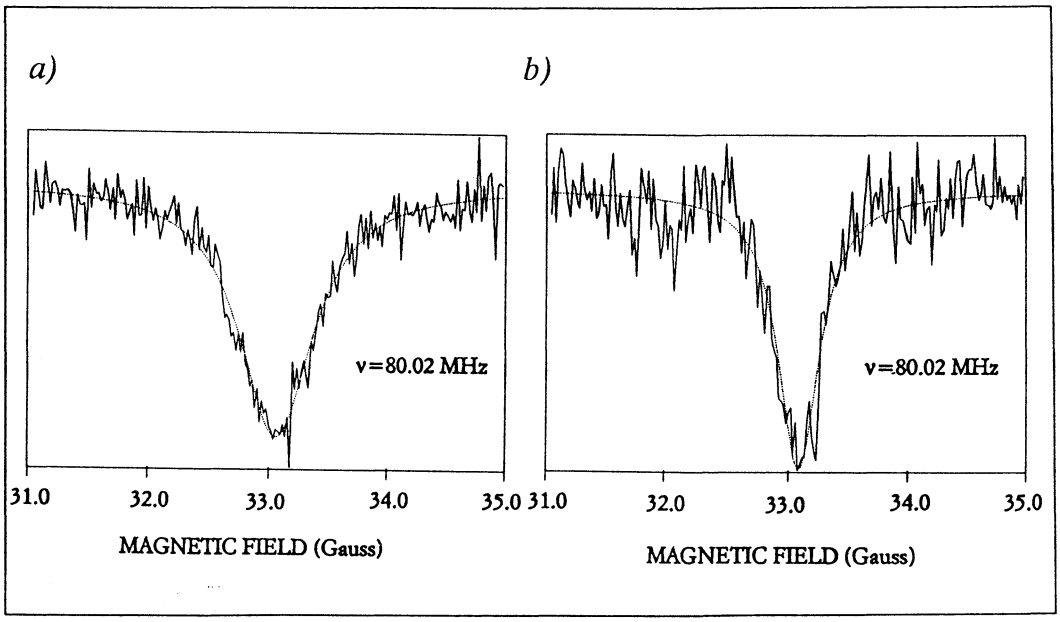

Fig. 3.5.3. a) The ODR signal without delayed detection. b) The ODR signal with 650 ns delayed detection.

REFERENCES

1. S. Svanberg: Atomic and Molecular Spectroscopy: Springer-Verlag, Heidelberg

2. J. Bengtsson, J.Larsson, S. Svanberg, C.-G. Wahlström: Phys. Rev. **A41**, 223 (1990)

3. J. Bengtsson, J. Larsson, S. Svanberg: Phys. Rev. **A42**, 5457 (1990)

4. G.J. Bengtsson, J. Larsson, S. Svanberg, D.D. Wang: Phys. Rev., to appear

5. S. Garpman, G. Lidö, S. Rydberg, S. Svanberg: Z. Physik **247**, 238 (1971)

6. A. Kastler, J. Brossel: Compt Rend. **229**, 1213 (1949)

7. J. Brossel, F. Bitter: Phys. Rev. **86**, 368 (1952)

8. S. Garpman, L. Holmgren, A. Rosén: Phys. Scr. **10**, 221 (1974)

10. U. Berzinsh: Ph.D. Thesis, University of Latvia (Riga, 1988)

11. A. Ubelis, U. Berzinsh: Phys. Scr. **34**, 805 (1986)

12. F. Schade Phys. Rew. **A41** 512 (1990)

13. M. von Ardenne: Tabellen zur Angewandten Physik, Band 2 (Berlin, 1964)

14. J.H. Macek Rev. Mod. Phys. **45** 553 (1973)